Received: 3 August 2021 | Revised: 19 January 2022 | Accepted: 20 January 2022 | Published on: 21 March 2022

DOI: 10.1002/mrm.29191

RESEARCH ARTICLE

Magnetic Resonance in Medicine

Susceptibility artifact correction in MR thermometry for monitoring of mild radiofrequency hyperthermia using total field inversion

Christof Boehm[1] | **Marianne Goeger-Neff**[2] | **Hendrik T. Mulder**[3] | **Benjamin Zilles**[2] | **Lars H. Lindner**[2] | **Gerard C. van Rhoon**[3] | **Dimitrios C. Karampinos**[1] | **Mingming Wu**[1]

[1]Department of Diagnostic and Interventional Radiology, School of Medicine, Technical University of Munich, Munich, Germany

[2]Department of Medicine III, University Hospital, LMU Munich, Munich, Germany

[3]Erasmus MC Cancer Institute, Rotterdam, The Netherlands

Correspondence
Mingming Wu, Department of Diagnostic and Interventional Radiology, School of Medicine, Ismaninger Str. 22, 81675 Munich, Germany.
Email: mingming.wu@tum.de; @MingmingWu10

Funding information
H2020 European Research Council, Grant/Award Number: 677661, ProFatMRI

Purpose: MR temperature monitoring of mild radiofrequency hyperthermia (RF-HT) of cancer exploits the linear resonance frequency shift of water with temperature. Motion-induced susceptibility distribution changes cause artifacts that we correct here using the total field inversion (TFI) approach.

Methods: The performance of TFI was compared to two background field removal (BFR) methods: Laplacian boundary value (LBV) and projection onto dipole fields (PDF). Data sets with spatial susceptibility change and B_0-drift were simulated, phantom heating experiments were performed, four volunteer data sets at thermoneutral conditions as well as data from one cervical cancer, two sarcoma, and one seroma patients undergoing mild RF-HT were corrected using the proposed methods.

Results: Simulations and phantom heating experiments revealed that using BFR or TFI preserves temperature-induced phase change, while removing susceptibility artifacts and B_0-drift. TFI resulted in the least cumulative error for all four volunteers. Temperature probe information from four patient data sets were best depicted by TFI-corrected data in terms of accuracy and precision. TFI also performed best in case of the sarcoma treatment without temperature probe.

Conclusion: TFI outperforms previously suggested BFR methods in terms of accuracy and robustness. While PDF consistently overestimates susceptibility contribution, and LBV removes valuable pixel information, TFI is more robust and leads to more accurate temperature estimations.

KEYWORDS

interventional, mild hyperthermia, motion artifact, MR thermometry, proton resonance frequency shift, susceptibility artifact, total field inversion

1 | INTRODUCTION

Mild hyperthermia (HT) treatment (40-44°C) of various cancer types has shown to sensitize tumors to radio- and chemotherapy, thus increasing the survival rate.[1] Regional heating of tissue can be induced with radiofrequency (RF) antennas that create a focus in the target area. This treatment modality has become part of clinical practice for the treatment of various cancer types, including the treatment of sarcoma patients and patients with cervical cancer.[2-4] To prevent tissue damage by overheating, many procedures rely on temperature probes that are placed intraluminally or superficially onto the skin. Sometimes, a catheter is inserted into the tumor. In addition to these limited local temperature information, the only feedback originates from the patient's complaint to feeling local heat. MR temperature mapping can provide the required tissue coverage to detect unwanted hot-spots, and to monitor whether the desired thermal dose is applied to the tumor.

MR temperature monitoring of aqueous tissue exploits the linear proton resonance frequency shift (PRFS) of water with temperature, that can detect relative temperature changes with regards to a reference image.[5-7] Using PRFS of water can lead to accurate temperature readings when other phase confounders are accounted for.[8]

The conductivity change of tissue with temperature leads to different phase offsets at different time points and thus to significant temperature estimation errors.[9] This becomes especially important in the context of mild regional heating as the heated volume is large and as a high accuracy of temperature estimation is important for the small temperature change. The double echo gradient echo (DEGRE)[9] scheme or a phase-cycled fast spin echo (FSE) sequence[10] can correct for the conductivity bias.

Spatiotemporal drift of the main magnetic field B_0 as a result of hardware heating and hardware instabilities may be misinterpreted as temperature change if not corrected for.[11] The installation of additional reference tubes in the scanned field of view (FOV) containing substances with negligible PRFS with temperature, such as oil or silicone, allows to detect the B_0-drift in these areas.[12] Signal outside the heated area had been used as a reference as well.[13] The field drift is subsequently extrapolated onto the scanned FOV and subtracted from the phase difference map. The concept of B_0-drift correction using magnetic field probes was shown previously[14] and applied more recently to evaluate the specific absorption rate using MR thermometry.[15] However, this setup requires additional hardware. Another approach suggested the acquisition of free induction decay (FID) signals across multiple channels and the use of coil sensitivity profiles to generate B_0-drift maps.[16]

Monitoring organs affected by periodic respiratory motion requires a high temporal resolution and thus oftentimes only allow for two-dimensional (2D) slice coverage.[17] Motion compensation techniques in the context of tissue ablation and mild HT using MR-guided high-intensity focused ultrasound (MRgHIFU) include the multi-baseline approach, which acquires a dictionary of images at different respiratory states that can be used as the best matching reference.[18-20] This addresses periodic tissue displacement during ablation using MRgHIFU in abdominal organs[21] as well as periodic B_0-fluctuations during mild HT using MRgHIFU in the head and neck region.[22]

Another approach used during MRgHIFU is referred to as the "referenceless" approach.[23] It uses the phase of the current image outside the heated area as reference and interpolates a smooth function for the phase distribution into the heated area.[24] It resolves both the motion problem from reference images acquired at a different motion state and B_0-drift simultaneously, but only works if the heating is spatially confined, which is not the case during mild regional RF-HT.

It has been shown previously, that respiratory-induced B_0-fluctuations are negligible during PRFS-based MR thermometry of mild RF-HT in the pelvic region.[25] The predominant artifact source here originates from dynamic changes of susceptibility distribution leading to dipole artifacts that propagate to neighboring tissues.[26] Due to intestinal motion, the paramagnetic gases and diamagnetic water tissue exchange position, and cause large susceptibility distribution changes during treatment. The observed field perturbation equals the susceptibility change map convoluted with a dipole kernel. Furthermore, moving air bubbles inside a cooling water bolus during MR temperature monitoring of thermal therapies lead to strong susceptibility artifacts.[25]

Recently, it was proposed to correct for both the susceptibility artifacts and the B_0-drift up to a spatially first-order phase distribution in PRFS-based MR thermometry by solving the Laplacian boundary value problem (LBV)[27] or by projection onto dipole fields (PDF).[25,28] These two methods are well known in the context of quantitative susceptibility mapping (QSM) for separating the foreground from the background fields and were demonstrated to be advantageous in comparison to other background field removal (BFR) methods.[29,30] PDF is formulated as an optimization problem where the magnetic field inside the foreground mask is minimized by placing origins of dipole fields into a background mask. LBV solves the Laplace operator at the interface between foreground and background under the assumption that the field contributions at this layer of pixels originate only from the background field. However, PDF is known to overestimate the

background field, especially at air–tissue interfaces.[29,31] The LBV-based BFR method removes at least one pixel layer at the air–tissue border in order to calculate the Laplace operator, resulting in a loss of valuable temperature information.

Total field inversion was introduced for QSM and improves the quality of the QSM maps by incorporating background and local field estimation in one single step.[31-33] In this paper we applied TFI to DEGRE data acquired during mild RF-HT to correct for motion-induced susceptibility artifacts and resolve B_0-drift. We show that TFI can overcome the problem of PDF to overfit the background phase contribution as well as the problem of LBV to erase one pixel layer.

2 | METHODS

2.1 | MR thermometry

The phase difference from DEGRE was extracted as given in formula 1 in Reference 10. The resulting phase difference map to the reference time point was then unwrapped using the *unwrap_phase* method of the scikit-image python library (https://scikit-image.org/). The TFI and the BFR were then applied to the unwrapped phase as described in Reference 25. TFI and both BFR remove a spatially linear and constant phase distribution. This rendered the B_0-drift correction using the signal from reference tubes obsolete. However, as we observed a spatially constant temperature increase within the sarcoma and seroma patient, and a spatially linear temperature increase in the phantom experiment, we used the signal within the reference tubes to discern temperature and B_0-drift, as shown in Supporting Information Figure S1 of Reference 25. A polynomial function of first order was fit over the three-dimensional (3D) volume using the signal from all four vials for that purpose. In the following, we used the notation "B0-drift corrected" for this approach.

2.2 | Total field inversion

The total field inversion method consists of minimizing the following cost function:

$$y = \arg\min_{y'} = ||W(f - d * Py')||_1 + \lambda||M_G \nabla Py'||_1, \quad (1)$$

where $||\,.\,||_1$ is the ℓ_1-norm, W is the magnitude weighting, f is the unwrapped phase, d is the dipole kernel, $*$ denotes a convolution, P is the preconditioner, λ is the regularization parameter, M_G is the MEDI-like edge mask[34] and ∇ is the gradient operation.[35] The final QSM map was computed as $\chi = Py$. The estimated susceptibility distribution χ was forward simulated to a phase map and subsequently demodulated from the original phase map. By design, the preconditioner P implicitly distinguishes between regions of background and local susceptibility sources.[31] To distinguish between background and local regions (region-of-interest [ROI]), a binary mask M_i per time point was calculated based on the maximum intensity projection (MIP) across echo times thresholded at 10% of its maximum value. A foreground mask per time point was subsequently defined where both the aforementioned thresholded MIP and the MIP at the reference time point had enough signal. For the LBV method three pixel layers were eroded from the foreground mask to obtain robust results through subjects and anatomies. Outside M_i, the preconditioner was calculated as a continuous cubic decay fitted to background susceptibility values obtained by the PDF method[28] as proposed in Reference 36. Inside M_i, the preconditioner was set to 1. Consequently, the preconditioner was automatically adapted to the ROI. To obtain the edge mask M_G, the Sobel filter in all three spatial dimensions was applied on the MIP. The regularization parameter λ was determined by a normalized root mean square error (RMSE) analysis of the numerical simulation (see below) and set to 1 for all datasets. For the normalization the averaged Euclidean norm of the reference map was used. The processing was mainly performed in Python 3.8 and CuPy 8.3.0[37] on a NVIDIA GeForce GTX 1080 Ti. Only for LBV the Matlab implementation available from Cornell University (http://pre.weill.cornell.edu/mri/pages/qsm.html) was used. The Matlab function was called from Python using the Matlab Engine API for Python.

2.3 | Materials

The phantom heating experiment, the volunteer data sets as well as the cervical cancer RF-HT treatment were acquired on a 1.5T GE system (GE Discovery MR450w) in combination with a BSD2000-3D Sigma Eye MR-compatible RF applicator (PYREXAR Medical). The RF applicator consisted of 24 dipole antennas arranged in three rings of eight antennas. Water circulation was not turned on during the phantom measurement nor the volunteer study. Water was circulated during the patient treatment, but stopped during MR measurements to avoid flow artifacts as described in Reference 38. The sarcoma patients were monitored in a 1.5T Philips system (Philips Ingenia 1.5T) and treated using a Sigma Eye MR Universal, or the Sigma 30 MR (PYREXAR Medical) in case of the single-leg treatment. RF-immune thermistors with high-impedance carbon wires ("Bowman" temperature

probes[39]) with an accuracy of 0.1°C were used to validate MR thermometry data.

2.4 | Simulations

The effect of motion-induced susceptibility changes on the phase distribution by field disturbances were simulated with a numerical water phantom. A spherical change of susceptibility values from water to air was simulated in the image center. This corresponds to a temporal field difference between an air-filled sphere at a reference time point and a water-filled sphere at the current time point. A FOV = 150 × 150 × 150 mm, an isotropic voxel size = 1 × 1 × 1 mm^3 and a susceptibility of 9.44 ppm[40] for air in reference to water was used. A 3D temperature increase following a Gaussian profile with a peak value of 10°C and a standard deviation of 5 voxels was added to the image. Furthermore, a spatially variant 1st order phase was added to imitate B_0-drift.

2.5 | Phantom measurements

A 2D multislice DEGRE with slice-interleaved acquisition scheme was used to monitor temperature. Using the phase signal at both TEs compensated for conductivity change-induced phase offsets[9] (TR = 620 ms, 25 slices, total scan time = 83 s, TE_1 = 4.8 ms, TE_2 = 19.1 ms, matrix size = 128 × 128, FOV = 50 cm × 50 cm, flip angle = 40°, slice thickness = 10 mm, bandwidth = 325.5 Hz/px). A cylindrical phantom (with a diameter of 30 cm and a depth of 40 cm) consisting of demineralized water, "super stuff" (TX-151), a hydrophilic organic polymer solidifying powder, and NaCl, to mimick the electrical properties of human tissue was used, for details see Reference 10. The phantom temperature started at 20°C and 400 W heating was performed for 25 min. This was repeated twice to show repeatability. Within the phantom, temperature sensors were placed which served as a reference measurement for the MR-based temperature maps. The mean MR temperature and standard deviation at the sensors' tips was estimated within a region of interest with the size of 8 voxels.

2.6 | Volunteers

Single echo datasets were acquired in the pelvic region of four volunteers at constant temperature (three male, one female) adhering to local ethics regulations (TE/TR = 15 ms/21 ms, 20 slices, matrix size = 128 × 160, FOV = 50 cm × 50 cm, flip angle = 14°, slice thickness = 10 mm). As no temperature change was expected, the conductivity bias did not need to be considered, and thus, a double echo acquisition scheme was not required. Between the acquisition of the reference baseline scan and the second scan for calculating the temperature difference map we waited for 30 min. Any temperature change would result purely from motion-induced susceptibility artifacts.

2.7 | Patients

Patient treatment scans were performed with the approval of the respective local ethics board at two hospitals with specialization on the treatment of cervical tumors and sarcoma patients, respectively. The cervical tumor was treated with the aforementioned BSD2000-3D Sigma Eye applicator inside a 1.5T GE system. One patient with a sarcoma, and one with a seroma after surgical removal of the sarcoma in the thigh, were treated with a Sigma Eye MR Universal inside a 1.5T Philips system. Temperature probes were inserted within catheters into the tumor. Every 5 or 10 min the temperature probe was retracted and reinserted within the catheter to map the temperature distribution along the catheter. Another sarcoma patient was treated using a single-leg applicator (Sigma 30 MR) and no invasive temperature probe was inserted into the tumor. A DEGRE acquisition corrected for the conductivity bias. In the GE system the echo times were set to TE = [4.8, 19.1] ms, and TE = [4.60, 18.41] ms in the Philips scanner, respectively. Other sequence parameters were identical to the ones used for the phantom heating experiment. The total RF-HT treatment duration was about 90 min with an initial ramp-up time of 30 min and subsequent maintenance of the temperature of about 60 min. Depending on the scanning protocol, DEGRE scans were acquired. A detailed summary of the patient treatment scans is given in Table 1.

2.8 | L1 versus L2 norm

To compare the presently adopted ℓ_1 data consistency term to the previously proposed ℓ_2-based TFI,[31] both approaches were applied and compared with each other in two of the volunteer scans at constant temperature, one treatment of a sarcoma, and a treatment of a cervical tumor.

2.9 | Cumulative distribution function analysis

For the detailed analysis of the error distribution for cases where no or small temperature changes are expected, the cumulative distribution function can serve as the cumulative error and can be calculated as

TABLE 1 Overview on mild radiofrequency hyperthermia treatment details on patient data. One cervix cancer patient, two sarcoma patients and one seroma patient were included in this paper. Three out of four patients had a temperature probe placed inside the tumor that was matched with MR thermometry data. The retraction frequency describes how frequently the temperature probe was retracted and reinserted in order to map a one-dimensional temperature distribution. The respective echo times for the double echo gradient echo sequence are also given.

Tumor type	Applicator	MR system	Probes + retraction frequency	TE_1/TE_2 (ms)
Cervical tumor Figure 6	BSD2000-3D Sigma Eye applicator	1.5 T GE Discovery MR450w	1 (tumor) every 10 min	4.8/19.1
Seroma Figure 7	BSD2000-3D Universal applicator	1.5 T Philips Ingenia	1 (tumor) every 5 min	4.6/18.41
Sarcoma Figure 8	BSD2000-3D Universal applicator	1.5 T Philips Ingenia	1 (tumor) every 5 min	4.6/18.41
Sarcoma Supporting Information Figure S1	Sigma 30 MR Single leg applicator	1.5 T Philips Ingenia	none	4.6/18.41

$$\mathrm{cdf}(\Delta T) = \frac{1}{N}\sum_{i=0}^{N} n(\Delta T_i), \quad n(\Delta T_i) = \begin{cases} 1, & \Delta T_i \leq \Delta T \\ 0, & \text{else} \end{cases},$$

where N is the number of voxels and ΔT_i the estimated temperature at voxel i.

3 | RESULTS

3.1 | Simulations

The comparison of the three aforementioned susceptibility artifact correction methods in a numerical simulation revealed that all three methods can eliminate both the linear phase as well as the dipole, while preserving the simulated Gaussian heat distribution (Figure 1). The LBV method led to the least cumulative error and performed best. PDF and TFI performed similarly, as seen in the cumulative error plot and the cross-sectional slice. However, TFI performed best close to the air inclusion in the center while LBV eroded valuable pixel information, PDF showed residual artifacts at the air–water interface. However, the TFI-corrected map showed diagonal streaks of over-estimated temperatures originating from the simulated heating spot.

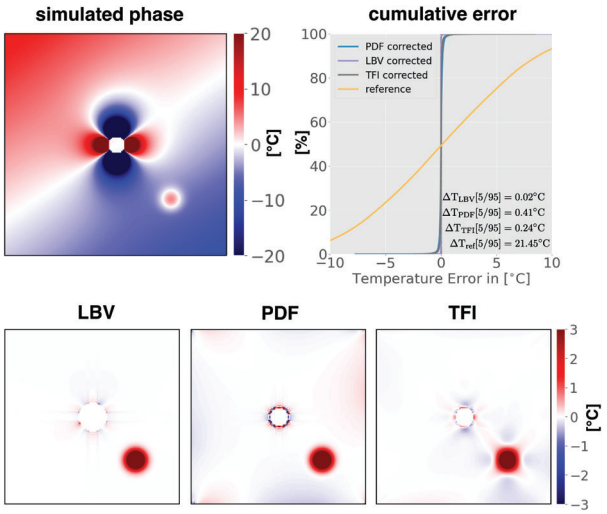

FIGURE 1 Results of temperature mapping in numerical simulations. The simulated phase included a Gaussian-shaped temperature change, as well as a dipole field caused by a moving air inclusion within surrounding water, and a first-order B_0-drift. The second row illustrates the corrected temperature difference maps, where B_0-drift and the susceptibility artifact have been removed, but the temperature was preserved. The Laplacian boundary value-based temperature map showed the least residual artifacts at the cost of a reduced region-of-interest, especially around the air inclusion in the center. Projection onto dipole fields and total field inversion (TFI) performed similarly, while the TFI-based temperature map showed less artifacts especially at the air–water interface in the center of the field of view. However, streaking could be observed for TFI. On the top right, the cumulative error is plotted for all cases.

3.2 | Phantom measurements

Temperature difference maps of the phantom heating experiment are shown in Figure 2. In addition, the local temperature estimation around two temperature sensor tips are plotted against the reference temperature probe data in Figure 3. In the beginning, as observed in the temperature maps, PDF overestimated the background field effect, which is particularly prominent at the border of the phantom (arrow). This was also reflected in

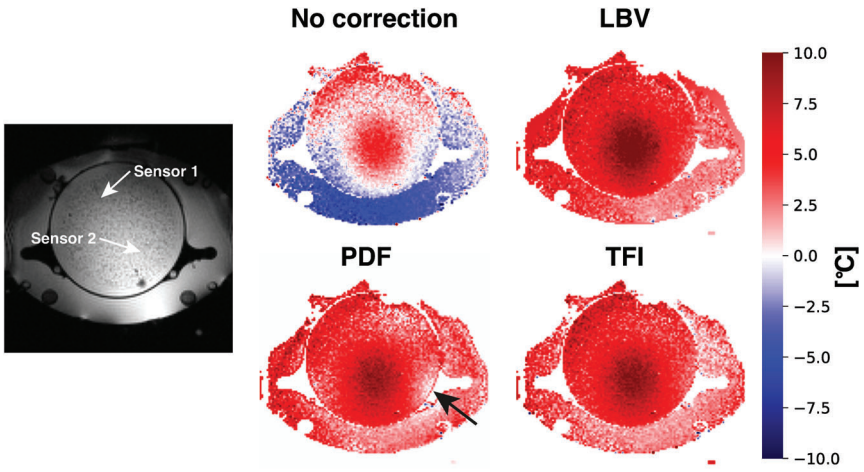

FIGURE 2 Results of temperature mapping in a gel phantom heating experiment. In general, all methods showed the highest temperature in the center of the phantom which was the selected target area for the heating microwaves. However, before correction, the temperature map was heterogeneous and showed unphysical negative temperature values, while the projection onto dipole fields-corrected temperature map showed decreased temperature values at air/phantom interfaces (arrow). Laplacian boundary value and total field inversion correction performed similarly and yielded homogeneous temperature maps.

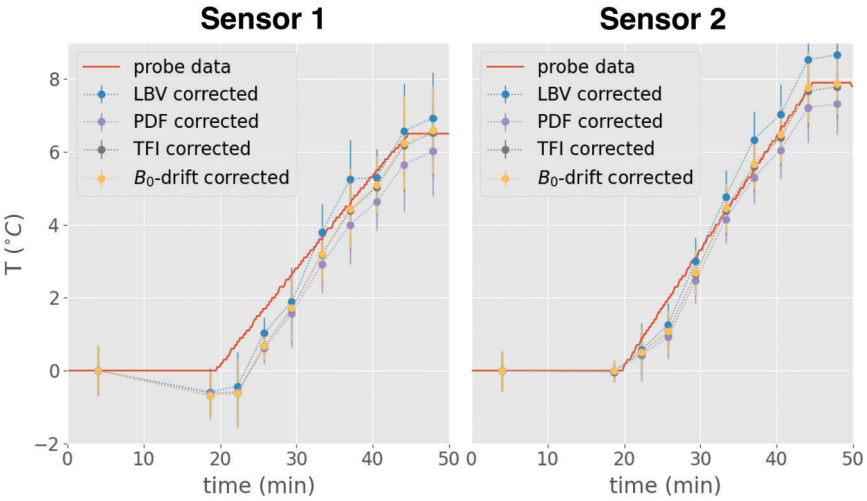

FIGURE 3 Correlation between sensors and MR temperature in the phantom depicted in Figure 2. Sensors 1 and 2 refer to the sensor position indicated in the magnitude image in Figure 2. A root mean square error analysis between MR temperature and sensor data yielded 0.61, 0.81, 0.69, 0.68 for Laplacian boundary value, the projection onto dipole fields method, total field inversion, and the B_0-drift corrected data in sensor 1, respectively, and 1.31, 0.59, 0.82, 0.88 in sensor 2. As seen, MR temperature mapping with susceptibility correction or B_0-drift correction was able to follow the trend of an increasing temperature for the phantom heating experiment.

the sensor matching data, where PDF-corrected MR data predominantly underestimated the temperature increase (Figure 2). At the same time, TFI underestimated the temperature, however, it followed the probe data more closely. At early time points, the LBV-corrected temperature was underestimated in reference to the probe data while overestimating at later timepoints. A RMSE analysis between MR data and probe data yielded 0.61, 0.81, 0.69, 0.68 for LBV, PDF, TFI, and the B_0-drift corrected data in sensor 1, respectively, and 1.31, 0.59, 0.82, 0.88 in sensor 2. It is to be noted, that the small RMSE differences between the methods remain difficult to interpret due to both a high spatial temperature distribution gradient and a residual uncertainty of the exact probe location. Yet, the phantom measurement has proven that all three methods successfully removed the B_0-drift effect while largely preserving the temperature-induced phase change, as the maps were in good agreement with the sensor probe data. However, when calculating the standard deviation inside the region of interest around the sensor probe, a smaller value could be observed for the BFR and TFI-corrected maps compared to the B_0-corrected maps, which can be explained by a subvoxel sinking of the phantom during the heating experiment and creation of small local dipoles that were corrected by both BFR and TFI.[25]

3.3 | Volunteers

The temperature difference maps of four volunteers at constant temperature showed strong susceptibility artifacts before correction (Figure 4). The artifacts were significantly reduced in the LBV- and PDF-corrected maps, but residual artifacts, especially in the water bolus at the posterior part of the image were visible. TFI was able to further reduce these artifacts and performs best in terms of cumulative error in all four volunteers (Figure 5). Furthermore, the TFI-corrected maps contained less noise. The characteristic of noise can best be assessed in the cumulative error plots, in which TFI showed the smallest interval between the 5 and 95 percentile for all subjects. The LBV-corrected maps showed a reduced remaining ROI due to the inherent need for erosion.

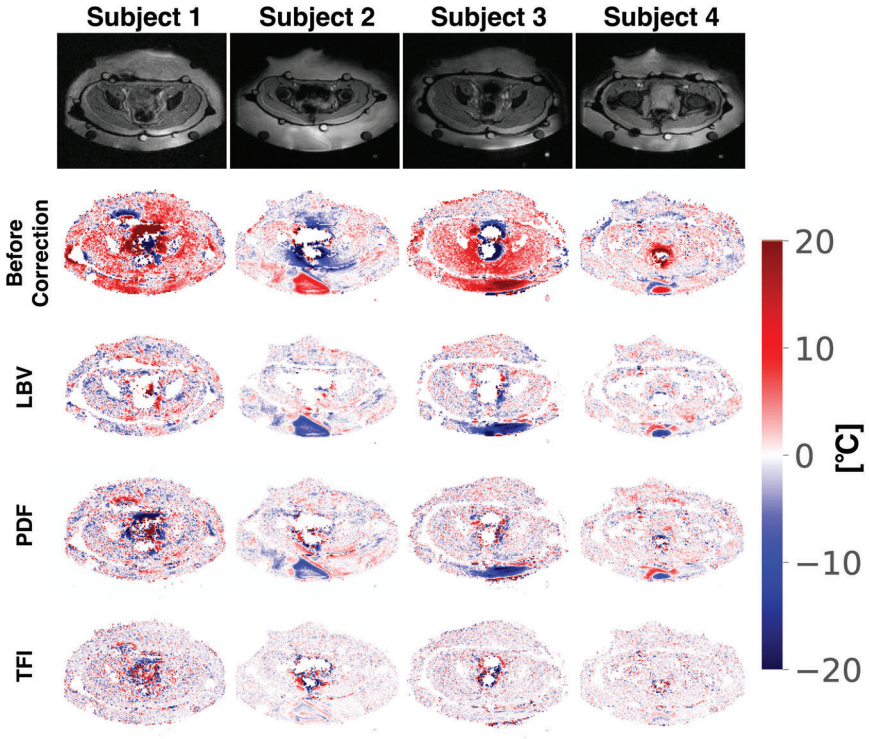

FIGURE 4 Results of temperature mapping in four volunteers at constant temperature. The temperature maps before correction showed strong bowel motion-induced susceptibility artifacts. While in subjects 2–4 residual artifacts remained especially in the posterior region, the total field inversion method was able to remove them.

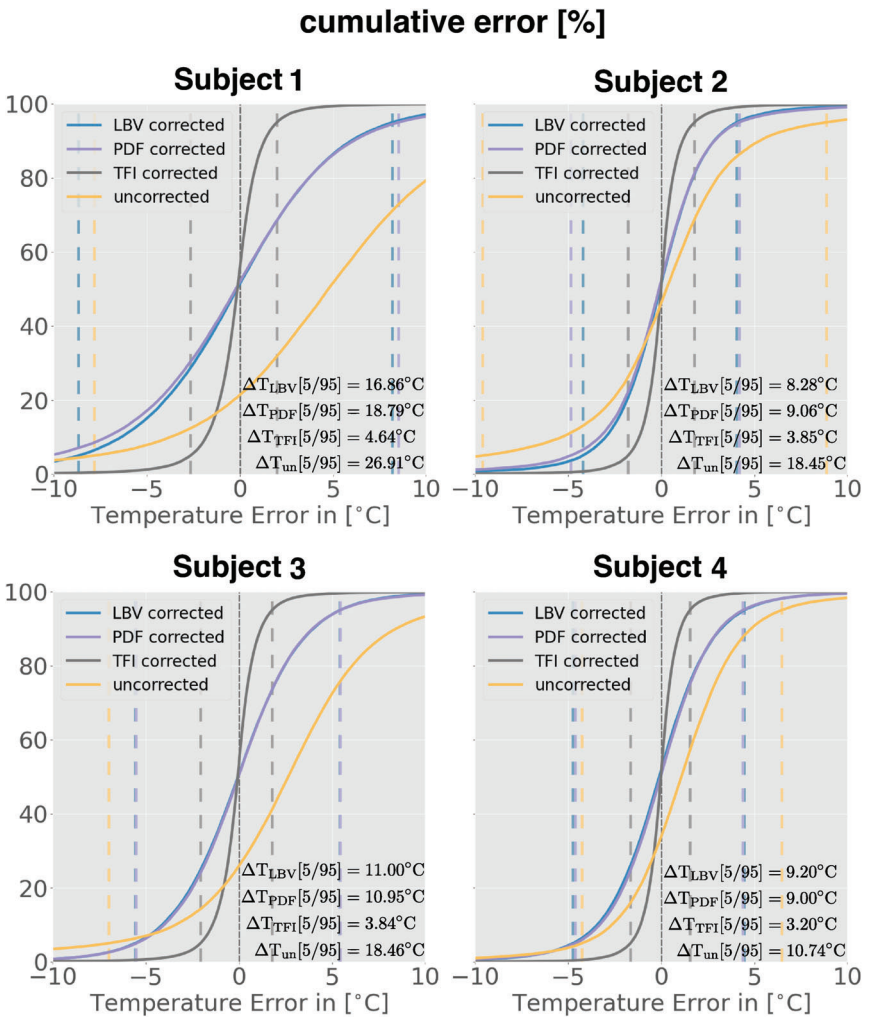

FIGURE 5 The cumulative error plots were calculated including all pixels within a common foreground mask. The plots indicate that total field inversion results in the least residual phase error in all four volunteer datasets. For subjects 3 and 4, the projection onto dipole fields and Laplacian boundary value (LBV) method performed similarly and are thus displayed on top of each other. In contrast to the cumulative error plot from the simulated data (Figure 1), LBV was here more vulnerable to noise.

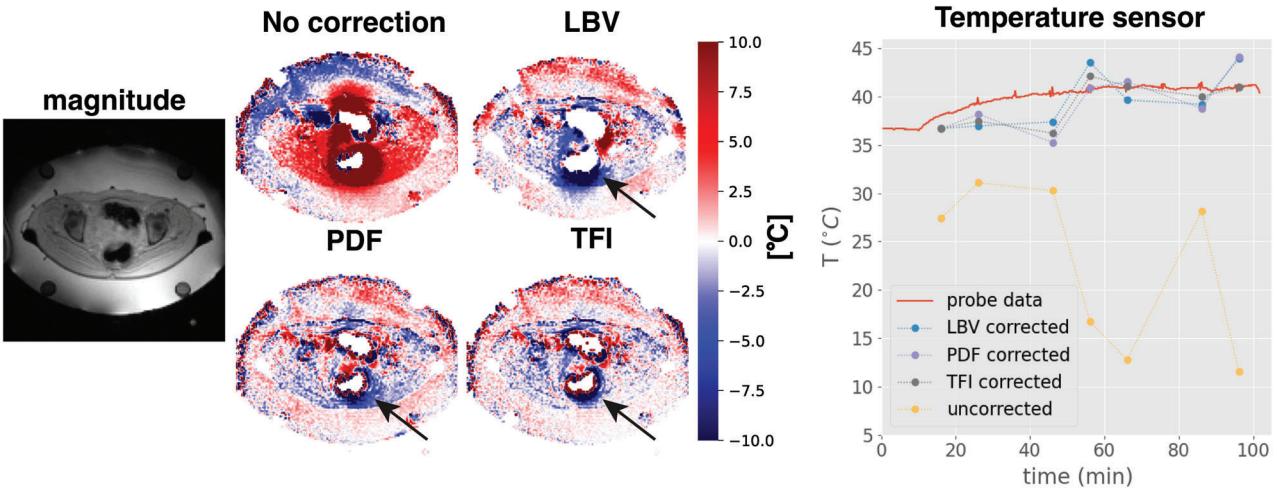

FIGURE 6 Results of temperature mapping for a cervical cancer patient during mild radiofrequency hyperthermia of the tumor. In the uncorrected temperature map strong susceptibility artifacts close to the intestines can be observed, caused by inter-scan gas motion. After correction the residual phase errors were reduced (arrows). However, the Laplacian boundary value (LBV) method was challenged with the removal of the error and dipole phase propagates into the surrounding tissue. While projection onto dipole fields could further reduce the range of the phase error it was minimal in the total field inversion-corrected map. Furthermore, the LBV method resulted in the loss of valuable pixels. The comparison of the corrected temperature with a sensor illustrates how severe the susceptibility artifacts were in the uncorrected DEGRE.

3.4 | Patients

The performance of the methods was evaluated for a mild RF-HT treatment of a patient with cervical cancer (Figure 6). Before susceptibility artifact correction, motion-induced temperature errors led to dipole-shaped artifacts amounting to more than 130°C and below −80°C locally. LBV could reduce the susceptibility artifacts at the cost of eroding pixel layers. PDF and TFI preserved the pixel information close to the air tissue interface, while TFI showed the smallest residual dipole artifact (arrow). Particularly noteworthy is that due to the spatial extension of the susceptibility artifact it propagated inside the silicone reference tubes. Hence, B_0-drift correction using the signal inside the reference tubes was not possible.

The temperature mapping results of the treatment of a patient with a seroma in the right thigh are shown in Figure 7. B_0-drift correction, LBV, PDF, and TFI yielded apparent sufficiently corrected temperature change maps and followed the trend of temperature increase over time compared to a temperature sensor inside the sarcoma. However, the coronal and sagittal view revealed two susceptibility artifacts (arrows) in proximity to the tumor and thus influencing temperature mapping accuracy. The dipole visible in the head direction of the FOV originated from bowel motion including gas and the dipole visible in the anterior part of the image in the sagittal views was introduced by a moving gas bubble inside the water bolus. In case of the LBV method, the axial and sagittal view revealed the estimation of unrealistic negative temperature values in the water bolus. PDF and TFI appear to remove all susceptibility artifacts and yielded a similar temperature map. On the right-hand side of Figure 7 the mean temperature is calculated over the tumor mask delineated with black lines in the views for the B_0-drift corrected maps. When correlating the mean temperature estimated via MR with the temperature sensor inside the tumor over time, the B_0-drift correction, PDF, and LBV yielded unstable results across time points, while the TFI-corrected temperature map followed the temperature sensor most accurately and robustly. A mean difference analysis of the the MR-based temperature with the sensor yielded −0.01°C for B_0-drift correction, −0.11°C for LBV, −0.21°C for PDF, and −0.40°C for TFI, while a RMSE analysis yielded 0.71°C for B_0-drift correction, 0.56°C for LBV, 0.57°C for PDF, and 0.49°C for TFI.

Figure 8 shows the temperature mapping results of the last time point of a patient with a sarcoma in the left thigh. B_0-drift correction, LBV and PDF were challenged in this subject and show a poor correlation with the temperature sensor. However, the TFI-corrected data is in good agreement with the temperature sensor. A mean difference analysis of the MR-based temperature with the sensor yielded 0.42°C for B_0-drift correction, −3.41°C for LBV, −3.57°C for PDF, and 0.09°C for TFI while a root mean square error analysis yielded 1.61°C for B_0-drift correction, 3.80°C for LBV, 4.05°C for PDF, and 0.21°C for TFI.

The significance of correcting for susceptibility artifacts also for regions distant to the intestines becomes apparent in another mild RF-HT of a sarcoma in the left

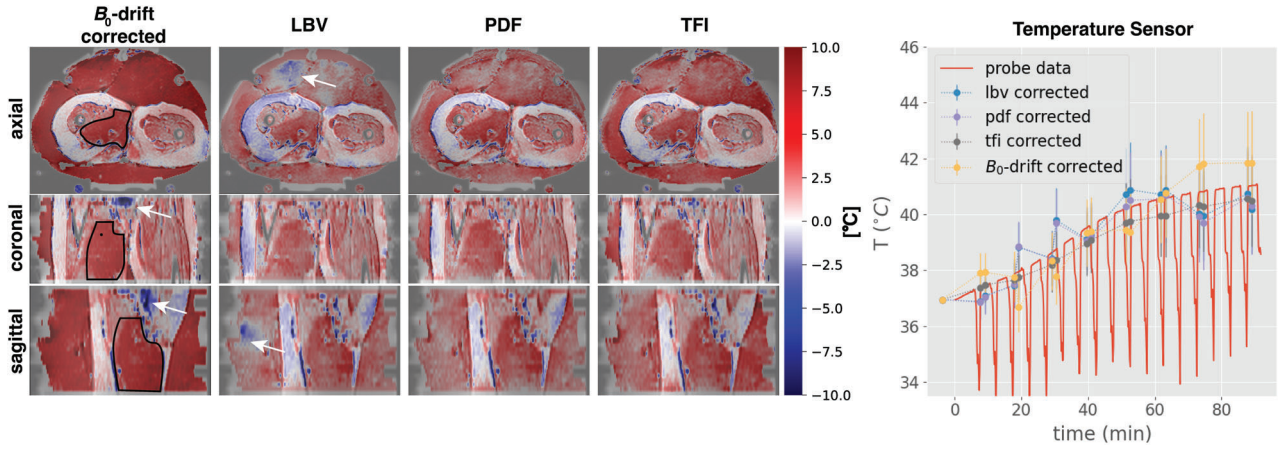

FIGURE 7 Temperature change maps derived from the last time point of a mild radiofrequency hyperthermia in a seroma patient after different correction schemes are shown on the left. The black line in the first column depicts the contours of the tumor in the right thigh. In the B_0-drift corrected temperature maps, a susceptibility artifact could be observed in the coronal and sagittal view (arrows). This susceptibility artifact was successfully removed in Laplacian boundary value (LBV)-, projection onto dipole fields (PDF)-, and total field inversion (TFI)-based maps. However, negative temperature value could be observed in the water bolus in the LBV-corrected maps. In the correlation between a temperature sensor within the seroma and the mean temperature in the tumor estimated by the different methods, the B_0-drift, LBV, and PDF corrected temperature values showed strong fluctuations and outliers between time points while the trend of temperature increase was picked up. Only the TFI-based temperature map correlated continuously across time points.

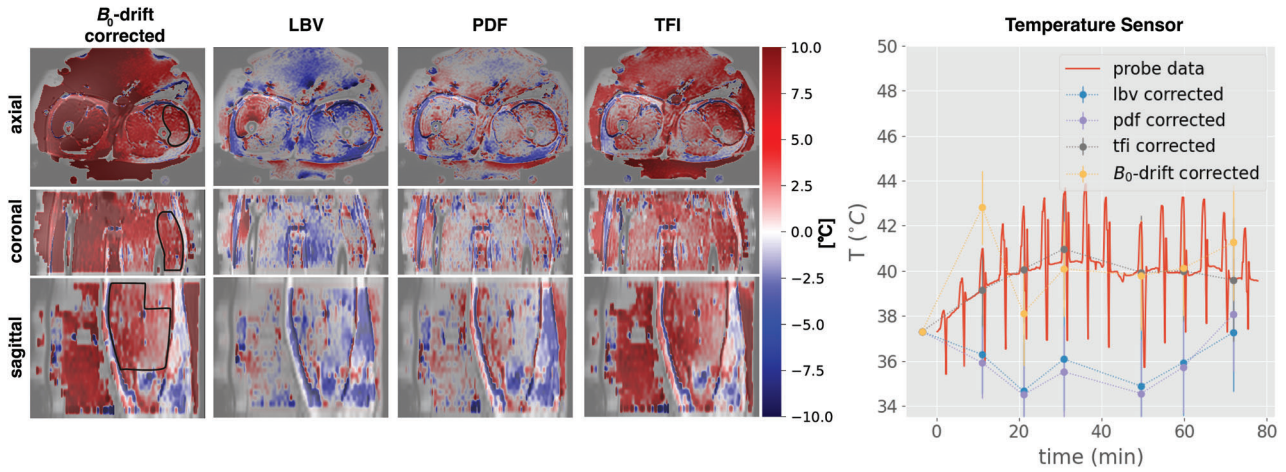

FIGURE 8 Temperature change maps derived from the last time point of a mild radiofrequency hyperthermia (RF-HT) targeting a sarcoma in the left thigh are shown. The contour of the tumor is depicted in the first column, on the B_0-drift corrected maps. The B_0-drift corrected map showed a residual first order variation in the right-left direction, while projection onto dipole fields (PDF) and especially Laplacian boundary value (LBV) showed predominantly negative temperature values in the entire FOV. Total field inversion (TFI) correction yielded consistently positive temperature values. The same was reflected in the probe matching evaluation on the right that reflect the temperature evolution over the time of the entire mild RF-HT. The mean temperature inside the tumor estimated with MR was compared to a reference temperature sensor using the mean value from signal inside the tumor region. In the correlation with a temperature sensor in the thigh, B_0-drift, LBV, and PDF correction showed heterogeneous values across time points, while TFI-corrected temperature points were in good agreement with the sensor.

thigh (Supporting Information Figure S1). The B_0-drift correction using the silicon reference tube signal failed to remove the first-order drift visualized in the axial view (arrow), as the susceptibility effects dominated the signal. Furthermore, strong susceptibility artifacts could be observed in the sagittal plane (arrows), originating from gas motion in the anterior part of the water bolus. LBV, PDF, and TFI successfully removed both the B_0-drift and the susceptibility artifacts. However, one susceptibility artifact remained across all method revealed in the coronal plane at the hollow of the knee (arrows). Furthermore, the PDF method yielded negative temperature at the air-bolus

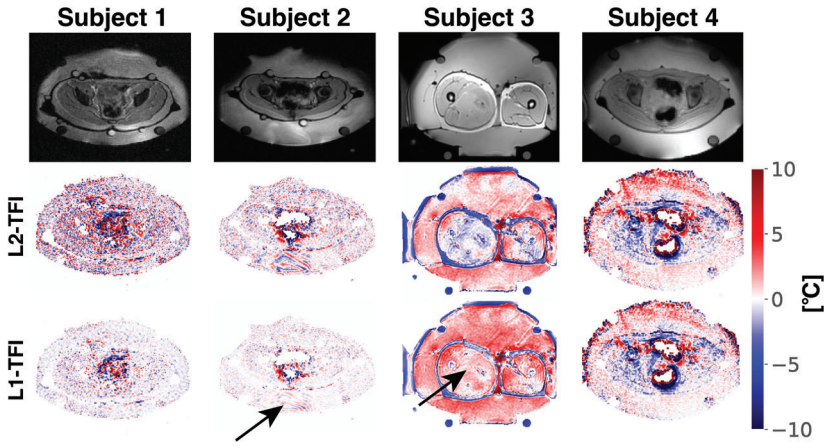

FIGURE 9 Results of temperature mapping in two volunteers (first two columns) and two patients (last two columns). Magnitude images (first row), corrected temperature maps based on the total field inversion method with an ℓ_2-based data consistency term (second row), and a ℓ_1-based data-consistency term (last row), are shown. In subject 1, the ℓ_1-based method was able to reduce the noise artifacts. In subject 2, the ℓ_1-based method reduced the noise artifacts as well as artifact in the posterior of the field of view (arrow). In subject 3, the ℓ_1-based method yielded positive temperature values within the right leg (arrow), while the ℓ_2-based map showed negative values. In subject 4, both methods performed similarly.

interface (axial view arrows), while TFI yielded the most homogeneous temperature map.

3.5 | L1 versus L2 norm

Figure 9 compares the performance of a ℓ_2 and the presently employed ℓ_1 data consistency term in the TFI cost function equation (1). In subjects 1 and 2 the ℓ_1 TFI reduced the background noise. In subject 2 the ℓ_1 TFI reduced the artifact in the posterior region almost to noise level (arrow). In subject 3, the ℓ_2 TFI-corrected temperature map showed nonphysical negative temperature values, which are estimated to be positive in the ℓ_1 TFI-corrected map (arrow). In subject 4 the two methods yielded almost the same temperature map.

4 | DISCUSSION

TFI-correction of MR thermometry data hampered by motion-induced susceptibility artifacts were superior to conventional B_0-drift corrected temperature maps and outperformed the recently proposed susceptibility artifact correction methods LBV and PDF in all examined data sets, except for the simulation data, where LBV revealed the least cumulative error after correction.

A TFI algorithm with a ℓ_1 norm data consistency term was proposed as it has proven to be more robust against phase inconsistencies and to perform better in low signal-to-noise ratio (SNR) regions in the domain of susceptibility mapping.[41] Furthermore, the proposed ℓ_1-based TFI algorithm was proven to perform more robustly in the presence of noise, as seen in the phantom and volunteer measurements and is thus in agreement with susceptibility mapping literature. This is advantageous in the context of mild RF hyperthermia treatments, as the heating device precludes the use of MR receive coils other than the body coil and thus suffers from low SNR. In contrast to LBV, TFI-corrected maps preserved all pixels. This is particularly useful in tumors that are located next to intestinal gas, and thus at the edge of the foreground mask, as it is the case for cervical or rectal cancer. Furthermore, TFI is known to be robust against the selection of a foreground mask[33] and enables a robust automatic mask generation based on a magnitude threshold across subjects and anatomies. The PDF method also preserves all pixels, however, it can suffer from its tendency to overfit, especially at air-tissue interfaces.

A B_0-drift with a spatial distribution following a first order polynomial is robustly removed using the proposed methods, as seen in the simulated data, the volunteer, and the pelvic tumor treatment. However, we observed a temperature rise following a spatially first-order polynomial for the phantom measurement and a spatially zeroth order polynomial (i.e., a constant temperature offset) for the patient heating data in the leg. To discern the contribution of temperature and the contribution of B_0-drift, we could use the signal within the silicon reference tubes (Supporting Information figure S1 in Reference 25). It is important to note that in presence of large susceptibility artifacts it becomes impossible to correct for B_0-drift by using the signal inside the reference tubes, which was the case both for the presented volunteer and patient scans in the pelvis. As the dipole-shaped artifact propagated to the reference tubes, fitting a first-order polynomial to only the reference tubes worsened the phase error. It is to be noted that a more efficient cooling during the cervical tumor treatment (water of around 20°C was used in comparison to 33°C in the sarcoma treatment) likely prevented a zeroth-order temperature rise in the data. B_0-drift correction methods for MR thermometry were proposed recently by acquiring additional FIDs[16] or using nuclear MR field probes.[15] In the absence of susceptibility change-induced dipole fields, both BFR and TFI can also remove a

spatially first-order B_0-drift, rendering aforementioned methods obsolete. Furthermore, the aforementioned methods would falsely identify the susceptibility change-induced dipole fields as B_0-drift, and a wrong field model would be applied, as neither the coil sensitivity profiles, in case of the FID acquisitions, nor the spherical harmonics functions, in case of the field probe approach, represent the dipolar field change correctly. The slow temperature increase during mild RF-HT allows for a low temporal resolution of the MR sequence, compared to MR monitoring sequences during ablation therapies. Thus, a large volume can be covered during imaging. This is needed to detect unintended hot-spots outside of the heating target. Moreover, it provides the phase distribution in 3D that is necessary to remove the susceptibility artifacts with high accuracy. Removing susceptibility artifacts from 2D data had been shown using PDF during ablation therapy, but is less robust.[17]

Crucial to PRFS-based MR thermometry that uses phase information are correctly represented phase maps. Influences from breathing-induced B_0 fluctuations in the pelvis were excluded in a previous study that showed the stabilizing effect of the water bolus on the phase signal.[25] This is partly explained by the restricting effects of the water bolus on respiratory motion, but mainly with the absence of susceptibility distribution changes: In absence of a surrounding water bolus, breathing would imply periodic susceptibility distribution change of tissue with air, causing periodic field perturbations. In the presence of the water bolus, tissue moves within the water bolus, leading to much smaller susceptibility distribution changes with time and thus the elimination of B_0-fluctuation inside the pelvis.

Certain limitations remain: GPU with at least 6GiB of RAM is needed for the processing to finish in a reasonable time frame. The processing of one time point took around 13, 6, and 25 s for TFI, PDF, and LBV, respectively, while only TFI and PDF used the GPU. Furthermore, intra-scan motion artifacts originating from bulk motion and intestinal gas motion affect image quality. These scans can be seen as outliers in the temperature quantification maps and need to be discarded or repeated. Inter-scan bulk motion occurs as neither the pelvis nor the legs are externally fixed. This leads to misalignment of the current phase map with the reference map. It was not observed in the datasets we presented in this paper, but can be solved by using the image after bulk motion as the reference for subsequent images and performing nonrigid image registration of the temperature maps as suggested in Reference 42. In our study, we did not optimize the MR sequence details for speed or temperature-to-noise ratio,[10] but evaluated data obtained with clinically established standard sequences.

5 | CONCLUSION

Susceptibility artifacts hamper MR temperature estimation during mild RF-HT in the pelvis and the legs due to motion of gas, inside the bowel due to digestion, or inside the cooling water bolus. These susceptibility distribution changes superimpose the temperature-induced phase change of 0.01 ppm/°C. LBV, PDF, and TFI successfully remove susceptibility artifacts while preserving the temperature-induced phase change, as seen in the simulation and the phantom heating experiment. For in vivo data however, TFI performed more robustly. In contrast to the PDF algorithm, TFI did not show the tendency to overestimate the background field contribution, and in contrast to the LBV method, TFI preserved all pixels, which was expected. Apart from the simulated dataset, TFI consistently outperformed both BFR methods. It resulted in the least cumulative error for the volunteer scans, and matched best to the reference temperature probe for all three patient treatments with a temperature sensor. TFI can thus be used for gaining accurate temperature maps during mild RF-HT treatments.

ACKNOWLEDGEMENT

Open Access funding enabled and organized by Projekt DEAL.

ORCID

Christof Boehm https://orcid.org/0000-0003-1321-5804
Hendrik T. Mulder https://orcid.org/0000-0003-2165-8840
Lars H. Lindner https://orcid.org/0000-0003-3708-8264
Gerard C. van Rhoon https://orcid.org/0000-0002-7365-5783
Dimitrios C. Karampinos https://orcid.org/0000-0003-4922-3662
Mingming Wu https://orcid.org/0000-0002-8593-7091

REFERENCES

1. Kampinga HH. Cell biological effects of hyperthermia alone or combined with radiation or drugs: a short introduction to newcomers in the field. *Int J Hyperth*. 2006;22:191-196.
2. Issels RD, Lindner LH, Verweij J, et al. Effect of neoadjuvant chemotherapy plus regional hyperthermia on long-term outcomes among patients with localized high-risk soft tissue sarcoma: the EORTC 62961-ESHO 95 randomized clinical trial. *JAMA Oncol*. 2018;4:483-492.
3. Bucklein V, Limmroth C, Kampmann E, et al. Ifosfamide, Carboplatin, and Etoposide (ICE) in combination with regional hyperthermia as salvage therapy in patients with locally advanced nonmetastatic and metastatic soft-tissue sarcoma. *Sarcoma*. 2020;2020:6901678.
4. Franckena M, Fatehi D, de Bruijne M, et al. Hyperthermia dose-effect relationship in 420 patients with cervical cancer

treated with combined radiotherapy and hyperthermia. *Eur J Cancer*. 2009;45:1969-1978.
5. Ishihara Y, Calderon A, Watanabe H, et al. A precise and fast temperature mapping using water proton chemical shift. *Magn Reson Med*. 1995;34:814-823.
6. Gellermann J, Hildebrandt B, Issels R, et al. Noninvasive magnetic resonance thermography of soft tissue sarcomas during regional hyperthermia: correlation with response and direct thermometry. *Cancer*. 2006;107:1373-1382.
7. Gellermann J, Wlodarczyk W, Hildebrandt B, et al. Noninvasive magnetic resonance thermography of recurrent rectal carcinoma in a 1.5 tesla hybrid system. *Cancer Res*. 2005;65:5872-5880.
8. Winter L, Oberacker E, Paul K, et al. Magnetic resonance thermometry: methodology, pitfalls and practical solutions. *Int J Hyperth*. 2016;32:63-75.
9. Peters RD, Henkelman RM. Proton-resonance frequency shift MR thermometry is affected by changes in the electrical conductivity of tissue. *Magn Reson Med*. 2000;43:62-71.
10. Wu M, Mulder HT, Zur Y, et al. A phase-cycled temperature-sensitive fast spin echo sequence with conductivity bias correction for monitoring of mild RF hyperthermia with PRFS. *MAGMA*. 2019;32(3):369-380.
11. ElSharkawy AM, Schär M, Bottomley PA, Atalar E. Monitoring and correcting spatio-temporal variations of the MR scanner's static magnetic field. *MAGMA*. 2006;19:223-236.
12. Poorter JD. Noninvasive MRI thermometry with the proton resonance frequency method: study of susceptibility effects. *Magn Reson Med*. 1995;34:359-367.
13. Bing C, Staruch RM, Tillander M, et al. Drift correction for accurate PRF-shift MR thermometry during mild hyperthermia treatments with MR-HIFU. *Int J Hyperth*. 2016;32:673-687.
14. Hernandez D, Kim KS, Michel E, Lee SY. Correction of B0 drift effects in magnetic resonance thermometry using magnetic field monitoring technique. *Concepts Magn Reson B Magn Reson Eng*. 2016;46B:81-89.
15. Ster CL, Mauconduit F, Mirkes C, et al. RF heating measurement using MR thermometry and field monitoring: methodological considerations and first in vivo results. *Magn Reson Med*. 2021;85:1282-1293.
16. Ferrer CJ, Bartels LW, van der Velden TA, et al. Field drift correction of proton resonance frequency shift temperature mapping with multichannel fast alternating nonselective free induction decay readouts. *Magn Reson Med*. 2020;83(3):962–973.
17. Tan J, Mougenot C, Pichardo S, Drake JM, Waspe AC. Motion compensation using principal component analysis and projection onto dipole fields for abdominal magnetic resonance thermometry. *Magn Reson Med*. 2019;81:195-207.
18. Vigen KK, Daniel BL, Pauly JM, Butts K. Triggered, navigated, multi-baseline method for proton resonance frequency temperature mapping with respiratory motion. *Magn Reson Med*. 2003;50:1003-1010.
19. Grissom WA, Rieke V, Holbrook AB, et al. Hybrid referenceless and multibaseline subtraction MR thermometry for monitoring thermal therapies in moving organs. *Med Phys*. 2010;37:5014-5026.
20. Wu M. *MR Thermometry for Monitoring mild Radio-Frequency Hyperthermia*. Dissertation. Technische Universität München, München; 2020.
21. Köhler MO, de Senneville BD, Quesson B, Moonen CT, Ries M. Spectrally selective pencil-beam navigator for motion compensation of MR-guided high-intensity focused ultrasound therapy of abdominal organs. *Magn Reson Med*. 2011;66:102-111.
22. Pichardo S, Köhler M, Lee J, Hynnyen K. In vivo optimisation study for multi-baseline MR-based thermometry in the context of hyperthermia using MR-guided high intensity focused ultrasound for head and neck applications. *Int J Hyperth*. 2014;30:579-592.
23. Rieke V, Vigen KK, Sommer G, Daniel BL, Pauly JM, Butts K. Referenceless PRF shift thermometry. *Magn Reson Med*. 2004;51:1223-1231.
24. Salomir R, Viallon M, Kickhefel A, et al. Reference-free PRFS MR-thermometry using near-harmonic 2-D reconstruction of the background phase. *IEEE Trans Med Imaging*. 2012;31:287-301.
25. Wu M, Mulder HT, Baron P, et al. Correction of motion-induced susceptibility artifacts and B0 drift during proton resonance frequency shift-based MR thermometry in the pelvis with background field removal methods. *Magn Reson Med*. 2020;84:2495-2511.
26. Dadakova T, Gellermann J, Voigt O, et al. Fast PRF-based MR thermometry using double-echo EPI: in vivo comparison in a clinical hyperthermia setting. *MAGMA*. 2015;28:305-314.
27. Zhou D, Liu T, Spincemaille P, Wang Y. Background field removal by solving the Laplacian boundary value problem. *NMR Biomed*. 2014;27:312-319.
28. Liu T, Khalidov I, de Rochefort L, et al. A novel background field removal method for MRI using projection onto dipole fields (PDF). *NMR Biomed*. 2011;24:1129-1136.
29. Schweser F, Robinson SD, de Rochefort L, Li W, Bredies K. An illustrated comparison of processing methods for phase MRI and QSM: removal of background field contributions from sources outside the region of interest. *NMR Biomed*. 2017;30:(e3604).
30. Ozbay PS, Deistung A, Feng X, Nanz D, Reichenbach JR, Schweser F. A comprehensive numerical analysis of background phase correction with V-SHARP. *NMR Biomed*. 2017;30:e3550.
31. Liu Z, Kee Y, Zhou D, Wang Y, Spincemaille P. Preconditioned total field inversion (TFI) method for quantitative susceptibility mapping. *Magn Reson Med*. 2016;78:303-315.
32. Wen Y, Spincemaille P, Nguyen T, et al. Multiecho complex total field inversion method (mcTFI) for improved signal modeling in quantitative susceptibility mapping. *Magn Reson Med*. 2021;86(4):2165–2178.
33. Boehm C, Sollmann N, Meineke J, et al. Preconditioned water-fat total field inversion: application to spine quantitative susceptibility mapping. *Magnet Reson Med*. 2022;87(1):417-430.
34. Liu T, Liu J, de Rochefort L, et al. Morphology enabled dipole inversion (MEDI) from a single-angle acquisition: comparison with cosmos in human brain imaging. *Magn Reson Med*. 2011;66:777-783.
35. Wang Y, Liu T. Quantitative susceptibility mapping (QSM): decoding MRI data for a tissue magnetic biomarker. *Magn Reson Med*. 2014;73:82-101.
36. Liu Z, Wen Y, Spincemaille P, et al. Automated adaptive preconditioner for quantitative susceptibility mapping. *Magn Reson Med*. 2020;83:271-285.

37. Okuta R, Unno Y, Nishino D, Hido S, Loomis C. CuPy: a NumPy-compatible library for NVIDIA GPU calculations. Proceedings of the 31st Annual Conference on Neural Information Processing Systems (NIPS) Workshop on Machine Learning Systems (LearningSys); 2017.
38. Allen SP, Steeves T, Fergusson A, et al. Novel acoustic coupling bath using magnetite nanoparticles for MR-guided transcranial focused ultrasound surgery. *Med Phys*. 2019;46:5444-5453.
39. Bowman R. A probe for measuring temperature in radio-frequency-heated material (short papers). *IEEE Trans Microw Theory Techn*. 1976;24:43-45.
40. Collins CM, Yang B, Yang QX, Smith MB. Numerical calculations of the static magnetic field in three-dimensional multi-tissue models of the human head. *Magn Reson Imaging*. 2002;20:413-424.
41. Milovic C, Lambert M, Langkammer C, Bredies K, Tejos C, Irarrazaval P. QSM streaking suppression with L1 data fidelity terms. Proceedings of the 29th Annual Meeting International Society for Magnetic Resonance in Medicine; 2020:3257.
42. de Zwart JA, Vimeux FC, Palussiere J, et al. On-line correction and visualization of motion during MRI-controlled hyperthermia. *Magn Reson Med*. 2001;45:128-137.

SUPPORTING INFORMATION

Additional supporting information may be found in the online version of the article at the publisher's website.

Figure S1 Temperature change maps of the last time point of a patient treatment targeting a sarcoma using a single-leg applicator. The B_0-drift corrected map shows a residual first-order temperature change in AP direction and strong susceptibility artifacts at the anterior edge of the image originating from moving air inside the water bolus (see arrow in sagittal view). Laplacian boundary value (LBV)-, projection onto dipole fields (PDF)-, and total field inversion (TFI)-corrected maps show no B_0-drift artifact and removed the susceptibility artifacts in the anterior part of the image. However, some smaller residual dipole artifacts remain after correction (arrows in the coronal view) in all correction schemes. Again, an overestimation of the background field can be observed for PDF at the edge of the field of view (arrows in the axial view). The LBV-corrected maps also led to large areas with a negative temperature inside the water bolus and the fat.

How to cite this article: Boehm C, Goeger-Neff M, Mulder HT, et al. Susceptibility artifact correction in MR thermometry for monitoring of mild radiofrequency hyperthermia using total field inversion. *Magn Reson Med*. 2022;88:120-132. doi: 10.1002/mrm.29191